


Ameliorating Dust Mitigation on Solar Panels along with Drag Force Evaluation Utilizing Hybrid Coating to Repel Dust Particles from Photovoltaic Modules: An Experimental Analysis

Pooya Hooshyar¹, Hesam Moghadasi², Ali Moosavi*¹ , Parva Hooshyar³

¹ School of Mechanical Engineering, Sharif University of Technology, Tehran, Iran.

² Department of Mechanical Engineering, Faculty of Engineering, Arak University, Arak, Iran.

³ Department of Chemistry, Sharif University of Technology, Tehran, Iran.

ARTICLE INFO

Article Type

Original Research

Article History

Received: July 24, 2025

Accepted: September 02, 2025

ePublished: November 01, 2025

ABSTRACT

The performance and lifespan of photovoltaic (PV) systems are significantly affected by soiling dust, and atmospheric particle accumulation which reduces light transmission and energy output, especially in arid and semi-arid climates. This study introduces a hybrid anti-soiling coating that combines passive (surface modification) and active (electrostatic repulsion) mechanisms to enhance dust resistance on PV module glass. The coating, prepared via a sol-gel process using tetraethyl orthosilicate (TEOS), zinc acetate, monoethanolamine (MEA), and aluminum nitrate, was applied through dip coating. Field Emission Scanning Electron Microscopy (FE-SEM) imaging confirmed the presence of a thin, uniform layer suitable for light transmission and low resistivity. Optical analysis showed an average transmittance of 85.20% across 350–1000 nm wavelengths. Anti-soiling performance was assessed through repeated dust deposition and removal. Under a 50 kV/m electric field, dust removal efficiency improved steadily, with the resistance coefficient increasing from 93.0% to 97.1% over six cycles. Passive cleaning was also demonstrated through wind-based testing and image analysis, supported by drag force modeling showing effective detachment of larger particles. Simulations indicated smaller particles were less affected by airflow and needed electrostatic removal. A wind-flow simulation (5 m/s) on 60°-tilted panels tracked dust accumulation, aligning with experimental results. The hybrid coating resisted coverage loss and maintained performance over multiple cycles. This work demonstrates how combining electrostatic and surface engineered strategies can improve PV durability and self-cleaning, offering a scalable, cost-effective solution for dusty environments.

Keywords: Antisoiling, Hybrid dust repulsion methods, Photovoltaic module, Soiling, Solar panels.

How to cite this article

Hooshyar P, Moghadasi H, Moosavi A, Hooshyar P, Ameliorating Dust Mitigation on Solar Panels along with Drag Force Evaluation Utilizing Hybrid Coating to Repel Dust Particles from Photovoltaic Modules: An Experimental Analysis. Modares Mechanical Engineering; Eng. 2025;25(09):567-580.

*Corresponding author's email: Moosavi@sharif.edu

*Corresponding ORCID ID: 0000-0003-2346-963X



Copyright© 2025, TMU Press. This open-access article is published under the terms of the Creative Commons Attribution-NonCommercial 4.0 International License, which permits Share (copy and redistribute the material in any medium or format) and Adapt (remix, transform, and build upon the material) under the Attribution-NonCommercial terms.

1. Introduction

In recent decades, solar panels have played a pivotal role in advancing renewable energy, offering an environmentally friendly substitute for fossil fuels and supporting global carbon reduction initiatives. Technological progress in photovoltaic (PV) systems has notably enhanced their efficiency and reduced costs, facilitating their broad implementation worldwide. [1,2]. However, soiling, the accumulation of dust and other particles, remains a major challenge, obstructing sunlight, reducing energy output, and diminishing financial returns. Soiling is especially problematic in dusty, arid, or industrial areas, making effective mitigation crucial to maintaining energy generation and financial viability. To combat soiling, both passive and active dust mitigation strategies have been developed, each with distinct costs and benefits [3].

Passive dust mitigation approaches, such as hydrophobic and anti-reflective surface coatings, act by inhibiting the adhesion of dust particles to solar panels, thereby facilitating their removal by natural agents like wind or rainfall. [4,5]. Although these coatings involve an upfront application cost, they typically require minimal upkeep, which helps lower both the frequency of manual cleaning and water usage. [6,7] Nonetheless, they may degrade over time, requiring periodic reapplication, and tend to perform best under moderate dust exposure. Depending on the environmental context, passive strategies can decrease energy losses by approximately 15% to 30% [10,11], making them especially effective in regions with occasional rainfall, making them suitable for regions with some natural rainfall. Active dust mitigation techniques involve powered mechanisms and are often more effective but incur higher operational costs. [8–10]. Mechanical cleaning systems [11], including robotic wipers [12], brushes, and water jets [13], are commonly used in large solar farms. These systems can reduce soiling losses by up to 95% [9,14,15], particularly in arid areas without rainfall. However, they require substantial capital. [5,16], ongoing maintenance, and often water, which increases operational costs, especially in water-scarce regions [17]. Emerging active systems, like electrostatic cleaning, use electric fields to repel dust and avoid the need for water or direct contact, though they are still in development and need further evaluation for cost-effectiveness [18–20]. Generally, passive methods offer a lower total cost of ownership, while active methods provide higher dust removal efficiency. The choice between them depends on the site's environmental conditions. [21], resources, and budget [22]. Passive coatings suit humid areas with rainfall [23], whereas active systems are better for deserts with minimal natural cleaning. Despite these options, challenges remain in achieving cost-effective, high-performance dust mitigation for solar installations [24,25], especially in high-soiling regions.

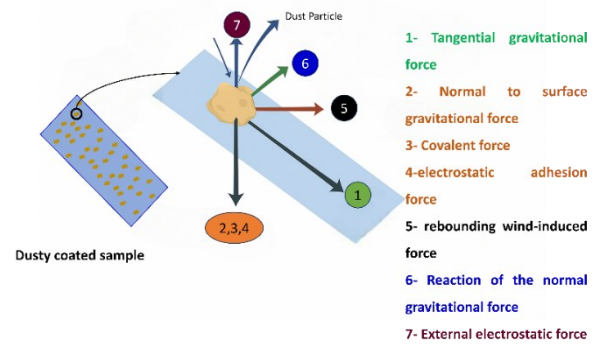


Fig.1. The acting forces on a dust particle placed at a coated substrate.

Continued innovation is needed to enhance the economic viability of solar power and address the persistent issues of dust accumulation and maintenance costs [26–29].

In this paper, a novel hybrid single layer coating is introduced which hires the advantages of both active and passive methodology as is depicted in Fig. 1. While the coating enhances the active electrostatic dust repulsion (with the Number 7), the antisoiling coating decreases the Covalent force (Number 3), electrostatic adhesion force (Number 4), and enhances the rebounding wind induced force (Number 5).

On the other hand, it is noted that the dust accumulation on the external surface of solar panels results in a condition commonly known as soiling, impacting their optical and thermal performance. Once dust particles settle on the panel surface, they impede part or all of the incoming solar radiation from reaching the PV cells. This results in a reduction of short-circuit current and, thus, in the overall system output power. In addition to the optical obstruction, dust particles can also alter the thermal properties of the surface by increasing surface absorption and localized heating, raising the temperature of the panel. Since PV efficiency tends to decrease with increasing temperature, such an effect also adds to performance degradation. The extent of loss in efficiency is determined by the composition, size, shape, and distribution of dust particles, as well as by environmental parameters such as humidity, wind, and frequency of natural or artificial cleaning. In desert and semidesert climates, where particulate matter in the air is greater, efficiency losses due to dust are greater than 20% if steps for mitigation are not implemented [3]. In order to visualize the workflow in this investigation, Fig.2 is presented.

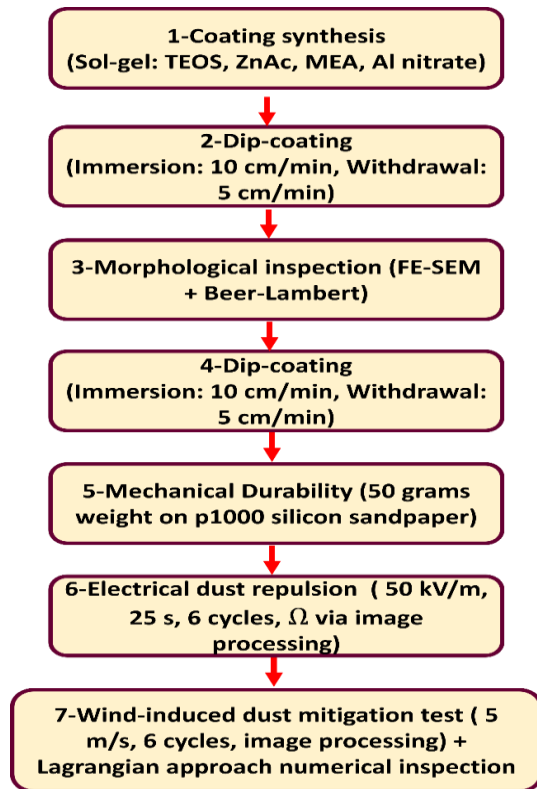


Fig.2. The followed steps in the current investigation.

Table.1. The uncertainty of the presented investigation

Parameter / Measurement	Main Source(s) of Uncertainty	Estimated Uncertainty	Impact on Results
Optical transmittance (UV-Vis)	Instrument baseline noise ($\pm 0.3\%$), wavelength accuracy (± 0.5 nm), repeatability	$\pm 0.5\%$ (combined)	Minimal; differences between coated/uncoated $> 5\%$
FE-SEM thickness measurement	Resolution limit of FE-SEM, thresholding in image analysis	± 3.5 nm	Negligible for overall conclusions
Mechanical abrasion test	Tolerance in applied load (± 0.05 g), stroke length control	$\pm 2\%$	Small variation in abrasion resistance trend
Wind-induced dust mitigation	Voltage fluctuation (± 0.5 kV/m), ambient humidity variation ($\sim 3\%$)	$\pm 3\%$	Minor variation in Ω values ($< 2\%$)
Numerical simulation	Wind speed control (± 0.05 m/s), image segmentation error ($\sim 1.2\%$)	$\pm 1.5\%$	Minor variation in soiling ratio trends
Numerical simulation	Assumptions in particle sphericity, density ($\pm 5\%$), drag coefficient correlation ($\pm 3\%$)	Up to $\pm 4\%$	Does not change qualitative conclusions

At last, all of the experimental and numerical inspections in this study are accompanied by uncertainties and errors, inevitably.

These regards are listed in Table.1.

2. Materials and test methods

All materials for the cleaning process and solution preparation were sourced from Merck, Germany, ensuring high purity and consistency. This included ethanol for cleaning, deionized water for rinsing, and hydrochloric acid (HCl) for pH adjustment. The sol-gel solution used tetraethyl orthosilicate (TEOS), zinc acetate, Monoethanolamine (MEA), and aluminum nitrate ($\text{Al}_2(\text{NO}_3)_3$) from Merck to maintain study reliability. Drying was done with either compressed air or laboratory-grade nitrogen gas.

2.1. Glass substrate preparation

The glass substrate started off with a good rinse using ethanol to get rid of any surface oils, dust, and other unwanted particles. If possible, we used an ultrasonic cleaner by submerging the substrate in ethanol and sonicating it for about 5 to 10 minutes to shake loose those more stubborn bits. After that, we rinsed the glass with deionized water to wash away any leftover ethanol, followed by a final rinse with ethanol to avoid any pesky water spots, thanks to ethanol's quick evaporation. For drying, we either used nitrogen gas or compressed air; if those weren't available, we popped the substrate in an oven set to $100\text{--}120^\circ\text{C}$ for 10 to 15 minutes. Once it cooled down, the cleaned substrate was all set for the dip-coating process.

2.2. Solution preparation

To prepare the final hybrid solution for dip-coating, a multi-step synthesis procedure was employed, involving the formulation of two precursor solutions with distinct functionalities. In the first step, Solution A was designed to provide passive dust mitigation properties, which was prepared by combining tetraethyl orthosilicate (TEOS) with ethanol in an acidic environment. The acidity was adjusted using hydrochloric acid (HCl) to control the hydrolysis and condensation rates of TEOS. This mixture was then stirred at 70°C for 1.5 hours, allowing the formation of a silica-based sol through sol-gel reactions. The resultant Solution A serves as the structural matrix of the coating and introduces surface characteristics such as increased roughness or hydrophobicity that contribute to passive dust repellence, especially under the influence of external forces like wind. In parallel, Solution B, responsible for the active dust mitigation mechanism, was formulated by dissolving zinc acetate in ethanol. Previously, ethanol was pre-mixed with monoethanolamine (MEA) at a concentration of 0.2 M, which serves as a stabilizer and complexing agent. To enhance the functionality of this solution, aluminum nitrate was added in a weight ratio of 0.3 relative to zinc acetate. The inclusion of

aluminum ions can influence the electronic and surface charge properties of the coating, enabling electrostatic interactions with dust particles. This active functionality is crucial in conditions where environmental factors such as wind are minimal, as it allows for dust mitigation via electrostatic repulsion or particle destabilization mechanisms. Following their preparation, Solutions A and B were combined and stirred at room temperature for 5 hours, yielding a homogeneous Solution C, which was subsequently used in the dip-coating process to fabricate the functional surface. The final coating thus integrates both passive and active dust mitigation strategies. Under windy conditions, the passive characteristics originating from Solution A facilitate dust removal by reducing particle adhesion and promoting wind-assisted detachment. In contrast, during calm weather conditions, where wind-induced forces are negligible, the active features, introduced through Solution B, take effect by interacting electrostatically with dust particles, helping to dislodge or prevent their accumulation. This hybrid approach ensures reliable and continuous self-cleaning performance of the coated solar panel across a variety of environmental scenarios, enhancing its long-term efficiency and reducing the need for manual cleaning interventions.

2.3. Dip-coating process

The dip-coating technique employed in this study involved controlled immersion and withdrawal speeds to ensure uniform film deposition. During the coating process, the glass substrate was submerged in the prepared solution at a constant downward speed of 10 cm/min. After reaching the desired depth, it was withdrawn vertically at a slower, regulated rate of 5 cm/min. These specific speeds were selected to balance coating thickness, adhesion quality, and surface uniformity based on the fluid properties and desired application performance. Fig.3 illustrates this procedure, schematically.

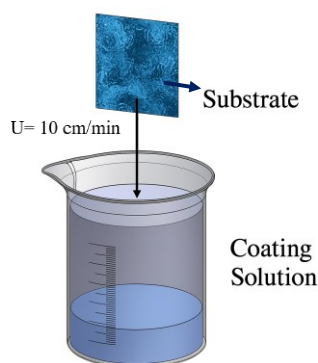


Fig.3. The dip-coating procedure.

3. Experiment design and numerical background

In the current work, the overall research strategy was seriously structured into two general branches, numerical analysis and experimental characterization, both of which consisted of a number of associated steps. As detailed in section 2, the coating material was synthesized by a multi-stage sol-gel route with TEOS, zinc acetate, MEA, and aluminum nitrate and subsequently deposited homogeneously onto lime glass substrates by a regulated dip-coating route (immersion at 10 cm/min and withdrawal at 5 cm/min). The experimental process began with morphological and structural verification of the coating using Field Emission Scanning Electron Microscopy (FE-SEM) for surface uniformity and thickness determination, complemented with non-destructive optical thickness mapping by applying the Beer-Lambert law to ensure homogeneity. Mechanical strength was subsequently tested using a sandpaper abrasion technique on 1000-grit silicon carbide paper under a constant normal load of 50 g in up to eight reciprocating 10 cm cycles to simulate long-term wear due to dust-induced micro-scratches in real PV applications. The same samples were then tested in two different anti-soiling performance tests sequentially after abrasion:

- (1) Electrostatic dust repulsion in which kaolin-contaminated samples were exposed to a steady electric field (50 kV/m for 25 s/cycle) in six successive cycles, and the efficiency of the removal of the dust was evaluated using Recovery in the Resistance Coefficient (Ω) via light transmission
- (2) Wind-blown dust reduction by coating that coated specimens exposed to six repeated wind-blow cycles at 5 m/s, soiling ratios determined by image-analysis measurements of particle coverage before and after each cycle.

The numerical component was meant to complement the experiments and consisted of a Lagrangian particle-track simulation to evaluate wind-displaced dust reduction under typical installation geometry (60° panel orientation). Vertical settling velocities were calculated from Stokes' law, and horizontal velocity components from particle-characteristic drag coefficients, enabling collision probabilities and surface coverage to be determined. In addition, a complete aerodynamic drag force calculation was performed for spherical dust particles of submicron to 10 μm radius utilizing both low-Reynolds Stokes-flow relations and transitional-regime drag equations. This integrated experimental-numerical approach provided the complete assessment of coating durability, optical stability, and concurrent two-mode dust suppression performance without invoking statistical optimization techniques such as Taguchi methodologies because the research was focused on deterministic physical modeling and simple performance validation in controlled conditions.

4. Characterization approaches

4.1. Surface morphology

Field Emission Scanning Electron Microscopy (FE-SEM) is a key technique for analyzing the surface morphology of thin films deposited on glass substrates. It uses a focused electron beam to generate high-resolution images of the film's microstructure, thickness, and surface uniformity. FE-SEM provides detailed insights into film quality, including features such as porosity and defects, making it invaluable for optimizing deposition processes and enhancing material performance in applications like electronics and optics. In order to examine the quality of the coating applied to the surfaces, a MIRA3 TESCAN electron microscope from the Czech Republic was employed. Also, to enhance electrical conductivity for imaging, the surfaces were coated with a thin layer of gold. As depicted in Fig.1, the coating is produced on the glass substrate. The low thickness of the coating is well-suited for minimizing the electrical resistance due to the silica nanoparticles. The thickness characterization of the coating in Figs. 4 and 5 presents complementary information on the layer uniformity and quality of the silica-based coating. Fig. 4, with the FE-SEM picture, displays the microstructural morphology and provides a direct high-resolution visualization of the coating surface. The surface features observed reveal a generally uniform coverage with minute local fluctuations.

In contrast, Fig. 5 presents the thickness map from Beer–Lambert law-optical characterization as a spatially resolved optical thickness map of the full sample. The Beer–Lambert outcome is in agreement with the FE-SEM observation, confirming the presence of a homogeneously coated specimen with bunched thickness values falling within a narrow range. The optical thickness map shows minor thickness variations and surface undulations consistent with the microstructural texture evident in the FE-SEM image. Overall, the Beer–Lambert–based thickness mapping effectively complements this characterization by providing a non-destructive, wide-area measure of thickness, thus confirming the coating's homogeneity and highlighting localized deviations that can influence performance.

The schematic illustration of the mechanical abrasion test is depicted in Fig.6. Similar to the experiment conducted by Van and colleagues, silicon carbide 1000-grit sandpaper was used in this experiment. During the experiment, after placing a 50-gram weight on the coated glass sample, the samples were rubbed on the sandpaper in 10 cm cycles, with the number of cycles ranging from one to six. Also, readers can refer to Refs. [30–33] For more Information.

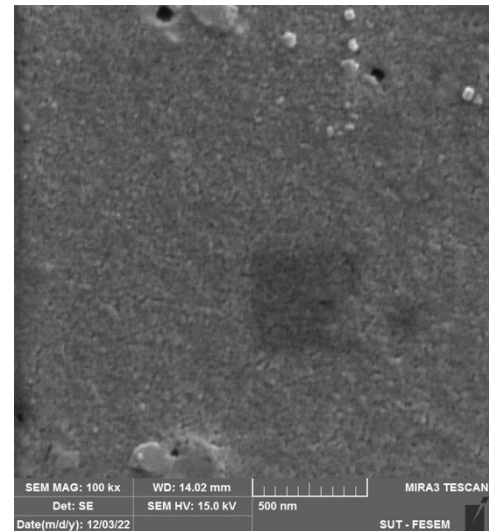


Fig 4. The FE-SEM image of the coated sample

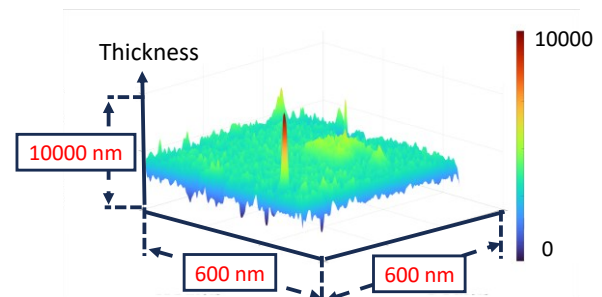


Fig.5. Beer-Lambert measurement of the coating.

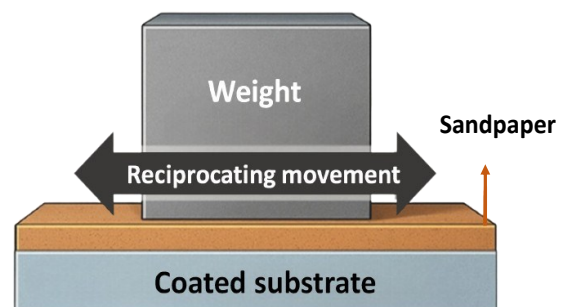


Fig. 6. The schematic of the mechanical abrasion test

4.2. Transparency and light transmission

This test was conducted using Avante's Avaspec-2048A. During the experiment, wavelengths ranging from 200 to 1000 nanometers were applied, and the ratio of received waves after passing through the coated surface to the initial waves was used to determine the light transmission of the coating.

Fig.7 presents the transparency of samples that were individually coated with conductive and anti-soiling layers across the previously specified wavelength range.

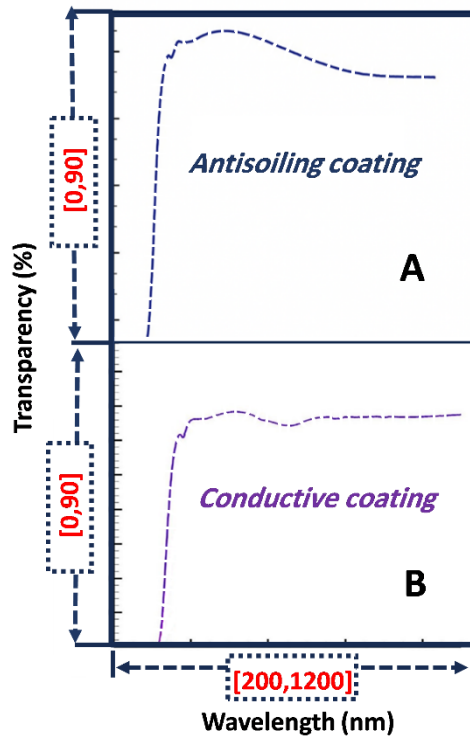


Fig. 7. The transparency of the coated samples. (A) Antisoiling coating, (B) Conductive coating.

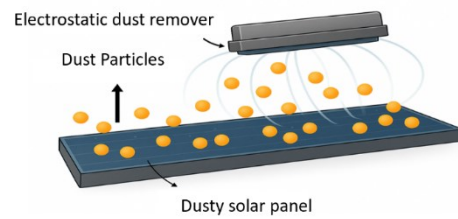
Finally, the coated sample showed 88.8% of transparency (1.5% higher than the uncoated glass substrate due to the anti-reflectivity properties) within this wavelength, on average

4.3. Investigation of electrical and anti-soiling dust repulsion

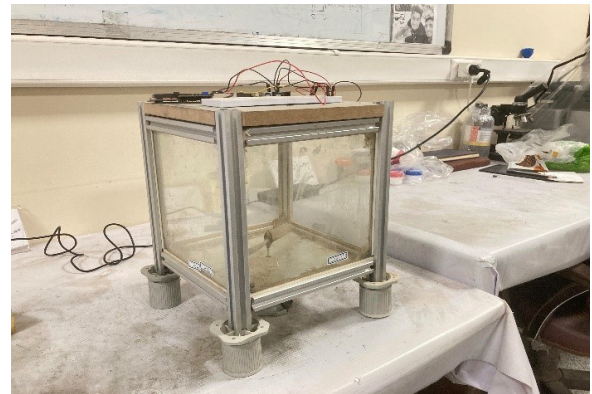
To evaluate the performance and functionality of the developed coating, a kaolin dust deposition test was conducted on the coated glass samples. This test is commonly employed to simulate environmental soiling and assess a material's anti-soiling and self-cleaning properties, particularly in outdoor applications like solar panels and optical devices.

Initially, both the coated and uncoated (bare glass) samples were subjected to kaolin dust exposure in a soiling chamber, as is depicted in Fig. 7. The level of transparency loss due to dust accumulation was measured using UV-Vis spectrophotometry or similar techniques. This comparison served to highlight the protective and anti-soiling capability of the coating by assessing how much less light the coated surface transmitted relative to its clean state, in contrast to the uncoated control sample.

Following dust exposure, the samples were cleaned using a stream of pressurized air at a pressure of 10 bar to simulate non-contact mechanical cleaning. However, to further examine the coating's electrostatic dust-repelling ability, the dusted samples were subsequently placed in an externally applied electric field



A



B

Fig. 8. A) The schematic of electrical dust repulsion [34]. The Soiling chamber used to settle dust particles on the coated substrates. B) Soiling chamber used to create dust fog

of 5 kV, with the electrode positioned at a distance of 10 cm from the surface. The presence of this field induces polarization or electrostatic forces on the dust particles and the surface, effectively weakening the adhesion between the particles and the substrate.

By comparing the amount of dust remaining on the surface before and after exposure to the electric field, the electrostatic cleaning efficiency of the coating could be quantified. This assessment offers insights into the potential of the coating to enable passive or active dust removal in real-world applications, thereby maintaining long-term transparency and performance.

The overall concept and mechanism of electrical dust repulsion involved in this test are schematically depicted in Fig. 8, providing a visual understanding of how the electric field interacts with the dust-covered surface to facilitate particle detachment and repulsion

As illustrated in Fig. 8B, the experimental setup incorporates a dedicated soiling chamber with an internal volume of approximately 8 liters, specifically designed to generate a uniform suspension, or dust fog, of kaolin particles. This controlled environment enables the reproducible deposition of particulate matter onto the coated test substrates. The dust fog is created by means of a mechanically driven impeller installed within the chamber, which is activated immediately after a predetermined quantity of kaolin powder is introduced through the chamber's inlet port. The impeller's rotation disperses the fine particles homogeneously throughout the chamber volume, simulating

atmospheric dust suspension. After a 3-minute mixing interval, the impeller is switched off to allow the system to return to a quiescent state. During this settling phase, the airborne particles gradually descend under gravitational influence, forming a consistent layer on the substrates positioned horizontally at the bottom of the chamber. This procedure ensures a controlled and repeatable soiling process, minimizing variability between test runs and facilitating reliable performance evaluation of the coatings under standardized particulate exposure.

4.4. Drag force evaluation on the dust particles

In this study, the aerodynamic drag force acting on dust particles was systematically evaluated to understand their potential for detachment under wind flow conditions commonly encountered in solar installations. The particles were modeled as spheres, and their interaction with airflow was analyzed over a wide range of sizes, from a few nanometers up to ten micrometers in radius.

The drag force exerted by the wind is strongly dependent on the particle size, the wind velocity, and the angle at which the wind strikes the particle. To account for this angular dependence, a variable drag coefficient was employed that reflects how the force distribution changes as the angle increases. Beyond a certain threshold angle, the force contribution was assumed to stabilize, mimicking the physical saturation observed in real-world conditions.

To quantify the effect of size, particles of different radii were examined, and the total aerodynamic force acting on each was calculated by integrating the angular contributions across the surface exposed to wind. The results indicate a clear trend: as particle size increases, the drag force increases significantly. This implies that larger particles are more easily mobilized by wind, while smaller particles remain more resistant to detachment due to their lower surface area and mass. This evaluation provides critical insight into the mechanics of passive dust removal. It reinforces the idea that wind-based cleaning mechanisms are more effective on coarse particulate contaminants, while additional methods may be required to remove fine particles that adhere more strongly to surfaces. Fig.9 schematically illustrates the 3D velocity field and pressure coefficient around a specific sphere in order to present the velocity field around a spherical domain.

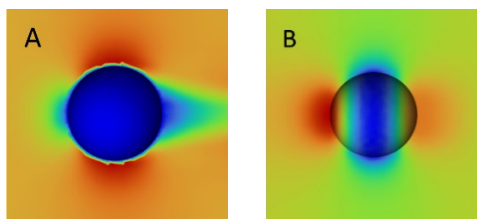


Fig.9. The 3D schematic of (A) velocity field around a sphere, (B) pressure coefficient. Both schematics are presented from a side view.

Fig.9. presents the flow characteristics around a spherical particle under uniform free-stream conditions, including the velocity field

(A) and the distribution of the pressure coefficient (B). These visualizations were generated to provide insight into the aerodynamic forces acting on dust particles subjected to wind flow, which is an essential consideration for passive self-cleaning mechanisms on exposed surfaces. In the velocity field (Fig. 9A), the presence of the sphere distorts the incoming flow, producing a stagnation point at the front of the sphere where the velocity drops to nearly zero. The flow accelerates around the curved surface, reaching maximum velocity near the lateral edges due to the local constriction, and eventually separates toward the rear, forming a low-velocity wake region. This wake zone is characterized by recirculation and reduced momentum, which plays a critical role in drag generation.

The pressure coefficient distribution (Fig.9 B) complements the velocity field analysis. A high-pressure region is observed at the stagnation point at the front of the sphere, gradually decreasing along the surface and reaching minimum values on the rear side, where the flow separation occurs. This asymmetric pressure distribution is the dominant contributor to the pressure (form) drag acting on the particle. The low-pressure wake at the rear of the sphere leads to a net aerodynamic force opposing the direction of motion.

Together, these two representations illustrate the mechanisms of drag force acting on dust particles. The combination of flow deceleration, pressure gradient, and wake formation defines the aerodynamic environment that affects the likelihood of particle detachment. The results emphasize the role of particle orientation and exposure in determining the magnitude and directionality of wind-induced forces in passive cleaning applications. As it is obtained from Fig.9, the distribution of the velocity field (and also the pressure field) around the domain causes a drag force that helps the dust particles to detach from the solar panels.

Fig.10 illustrates the coefficient local drag force around a dust particle radius of 10 μm . According to the fundamentals of this problem, while the boundary layer is stuck to the solid interface, the pressure coefficient can be calculated from Eq.1 [35,36]. When the boundary layer detaches from the interface, this coefficient becomes stagnant with its last value on the surface.

$$C_p = 1 - \frac{9}{4} \sin^2(\beta) \quad (1)$$

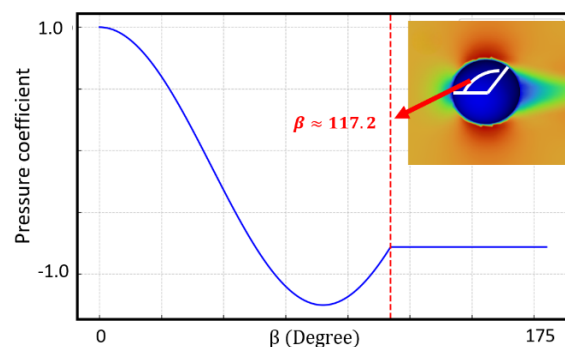


Fig.10. The local pressure coefficient on a dust particle with the wind velocity of 5 m/s.

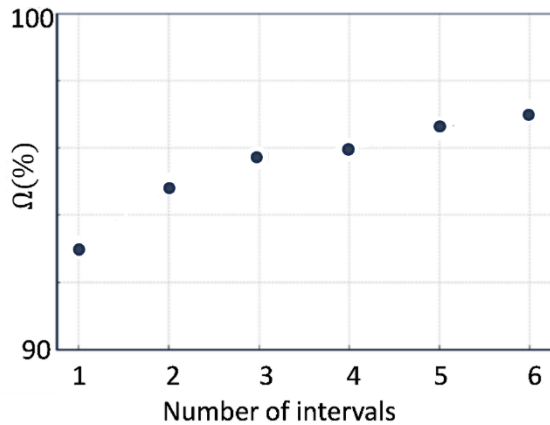


Fig.11. The Ω % for light transmission test.

According to Fig.10, integrating the curve yields the total drag force exerted on the aforementioned particle, which corresponds to the mathematical calculation of Eq.2.

$$F_D = \int \frac{1}{2} \rho V^2 C_p \sin(\beta) dA \quad (2)$$

In Eqs.2, F_D represents the total drag force exerted on the particle, ρ is the fluid density, C_p is the drag coefficient, β also describes the angular position on the surface according to Fig.10, and dA is the differential of the particle's surface area. On the other hand, since the drag force is highly dependent on the wind speed and the size of the dust particle, it is crucial to take this matter. To meet this end, Fig.10 provides the value of the drag coefficient over various sizes of dust particles in different wind speeds. The drag force experienced by a particle immersed in a fluid is primarily governed by the distribution of pressure and shear stress around its surface. In Fig. 10, the angular variation of the local drag force acting on a $10 \mu\text{m}$ dust particle is illustrated. This behavior is strongly influenced by the dynamics of the boundary layer that forms along the particle's surface. At the front region of the particle (near the stagnation point), the boundary layer remains attached to the surface. In this region, the pressure distribution follows a predictable analytical form based on classical low-Reynolds-number and potential flow theory, where the pressure decreases smoothly from the stagnation point as a function of the polar angle θ . This results in a characteristic drop in local drag force from the front toward the sides of the particle. As the fluid flows further along the particle surface, viscous effects dominate and may eventually cause the boundary layer to separate. This separation occurs at a critical angle, denoted in Fig. 10 as $\beta \approx 117.2^\circ$, beyond which the fluid streamlines can no longer adhere to the surface. Once separation occurs, the pressure distribution across the remaining rear surface of the particle tends to stagnate, maintaining approximately the same value as it had at the point of detachment.

5. Results and Discussion

As this test was conducted in 8 cycles of reciprocating back and forth movement, the dust repulsion ability of the coating is expected to reduce after each cycle. On the other hand, as the dust repulsion of the coating resists decreasing, the mechanical durability accounts for a better resistance coefficient (Ω). This coefficient can be calculated as follows:

$$\Omega(\%) = 100 \frac{\mu}{\sigma} \quad (3)$$

In the Eq.3, μ is the amount of dust removed from the surface, while, σ is presenting the amount of that poured on the surface initially.

5.1. Active electrical dust repulsion

Fig.11 illustrates the relative change percentage (Ω) of light transmission with different soiling periods. μ and σ represent the amount of dust removed from the surface and its initial value on the surface, respectively. Light transmission measurements were made across a broad spectrum of 350 nm to 1000 nm wavelengths. Results are presented as the ratio of the light intensity transmitted by the sample to the incident irradiance across the wavelength range. Throughout the test period, the coated sample also manifested a very high mean rate of light transmission at approximately 85.20%. This demonstrates the efficacy of the coating in maintaining optical clarity despite the deposition of soil and contaminants over time.

According to Fig.11, the relation provided in Eq.4 fits the data provided in this illustration with an accuracy of 96.2%.

$$\Omega(\%) = -0.2125 n^2 + 2.5218 n + 90.53 \quad (4)$$

In Eq.4, n represents the number of each interval.

5.2. Electrical dust repulsion

To evaluate the effectiveness and reproducibility of the electrical dust repulsion effect, a series of controlled experiments was carried out under a high-voltage electric field. The previously kaolin dust-deposited glass samples were subjected to an electric field with a strength of 50 kV/m for 25 seconds at each step. The cleaning process was performed in six consecutive periods, whereas during each of these, the remaining dust was eliminated electrostatically from the surface without any physical contact. After each cycle of repulsion, the optical performance of the sample was assessed through measurement of its residual clarity (Ω %), that is, the percentage transmission of light by the sample as compared to its clean and dust-free condition. The observations allowed the tracking of recovery of transparency after repeated repulsion occurrences. The results are summarized in Table 2 and graphically shown in Fig. 12, demonstrating a clear pattern of increasing transparency with each cycle. The sample coated attained a very high average light

transmission of approximately 95.52%, indicative of great dust removal capacity and sustained optical function after multiple uses. Fig. 12 shows the normalized electrical dust repulsion results. The percentage contribution of each of the resistance coefficients (Ω) of each of the intervals to the total dust removal ability across all six test cycles is given by each pie chart section. As observed, the highest percentages are the later intervals, particularly intervals 5 and 6, showing the progressive and even marginally enhanced efficiency of the coating over time in dust repulsion. This trend illustrates the material's reliability and performance consistency even through sequential soiling and electrical cleaning cycles. Although the preceding intervals were significant, the minimal Ω value increase per cycle reveals that the coating not only succeeded in retaining its functionality but likely also benefited from initial surface activation or conditioning effects. The general plot apparently shows a regular but increasing trend in dust removal efficiency, which further provides evidence of the hybrid coating towards long-term, maintenance-reduced performance under dusty environments.

Table.2. The Ω % after each electrical dust repulsion.

Number of intervals	Ω (%)
1	93.0
2	95.0
3	95.6
4	96.0
5	96.45
6	97.1

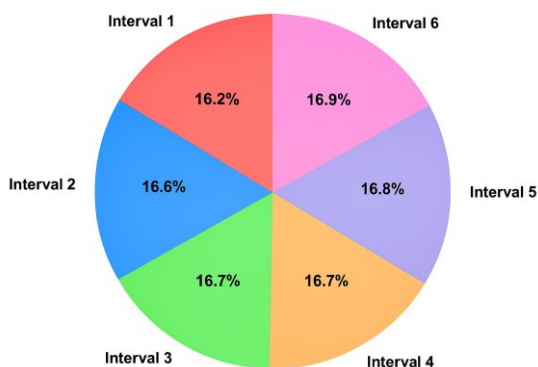


Fig.12. Normalized pie chart of Ω % after electrical dust repulsion.

5.3. Wind-induced dust repulsion

The inset in Fig. 9A and 9B visually captures this transition, showing the pressure field around the particle and the point of flow separation. The drag force profile reveals a steep decline in the front half, followed by a plateau after separation, highlighting the asymmetry introduced by the wake region. This asymmetric pressure distribution is a primary contributor to the net drag force acting on

the particle, and it plays a significant role in dust particle behavior, especially in electrostatic or flow-assisted cleaning applications.

The total drag force acting on the particle is obtained by integrating the local drag force distribution over the entire surface of the particle. As shown in Fig. 10, the curve represents the angular variation of the local drag force as a function of the polar angle θ . Therefore, the total drag force corresponds to the area under this curve, effectively capturing the cumulative contribution of differential forces acting at each angular position around the particle.

Mathematically, this integral accounts for both the magnitude and direction of the surface force components, weighted by their position on the particle. The asymmetry of the curve, particularly the stagnation of force values beyond the separation angle, reflects the imbalance between the upstream and downstream pressures, which is the primary source of the net drag force. As a result, Fig. 13 illustrates the average drag force applied by the fluid on the particle about the average Reynolds numbers, calculated based on the particle's radius (ranging from 0 to 10 μm). The data discuss the drag force (in units of 10^{-8} N) versus particle diameter (in micrometers) for various wind speeds ranging from 1.5 m/s to 7.0 m/s. The fluid medium is air, with a density of $\rho \approx 1.225 \text{ kg/m}^3$ and dynamic viscosity of $\mu \approx 1.81 \times 10^{-5} \text{ Pa}\cdot\text{s}$.

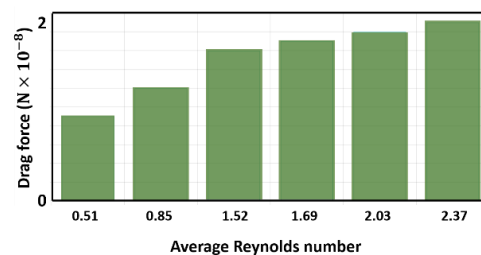


Fig.13. The variation of total drag force versus dust particle radius at different wind velocities ranging from 1.5 m/s up to 7.0 m/s.

Therefore, Fig. 13 presents the average drag force by the fluid on the particle versus the average Reynolds numbers, calculated in terms of particle radius, keeping in view the analysis performed here.

A decrease in the slope of the drag force found with increasing Reynolds numbers can be explained on scientific grounds by the transformation of the regimes of flow. With low Reynolds numbers ($\text{Re} \approx 0.51$ for 1.5 m/s), flow is laminar and viscous dominated, with the drag force following Stokes' law, $F_D = 6\pi\mu r v$, in a linear velocity- and particle-size-dependent way. When the Reynolds number increases (e.g., up to $\text{Re} \approx 2.37$ for 7.0 m/s), inertial forces become significant, and the drag force becomes nonlinear in velocity and diameter, according to the equation $F_D = (0.5C_D \rho V^2 A)$, where C_D is the drag coefficient and A is the cross-sectional area. The drag coefficient C_D decreases in this transitional regime, retarding the rate of increasing drag force, which manifests as a flattened slope in the

graph. This trend mirrors the early stages of flow transition from purely viscous to one where pressure drag and inertial effects balance the viscous component, according to aerodynamic theory for small particles in air under conditions studied

It is important to note that the thickness of the viscous boundary layer on the surface of the solar panel, approximately 3.27 mm at the downstream end according to classical boundary layer theory (Blasius and Pohlhausen solutions), is considerably larger than the typical size of airborne dust particles, which are usually in the micrometer range. This implies that dust particles near the surface reside well within the viscous sublayer, where no-slip boundary conditions and Stokes flow dominate.

Nevertheless, the present simulation does not focus on particles already deposited on or interacting directly with the surface within this viscous boundary layer. Instead, it considers only airborne dust particles suspended above the panel. A Lagrangian particle tracking method is employed, where particle trajectories are determined based on their initial velocity components, without resolving near-wall viscous flow or continuous particle-surface interactions. To determine the likelihood of dust particle collisions with the sample surface (as shown in Fig. 14), the vertical settling velocity is calculated using Stokes' law (Eq. 5), while the horizontal velocity is estimated via drag coefficients. Utilizing the Lagrangian coordinate framework, the model assesses particle impact probability based on these velocity components. This simplified aerodynamic model assumes particles fall ballistically toward the solar panel with predefined velocities, disregarding viscous drag, lift, or adhesion forces near the surface. Accordingly, the number of dust particles impacting the panel is evaluated based on their airborne kinematics rather than detailed boundary layer flow effects.

It is acknowledged that incorporating near-wall viscous interactions and particle-surface forces would provide more detailed insights and represent a valuable direction for future work.

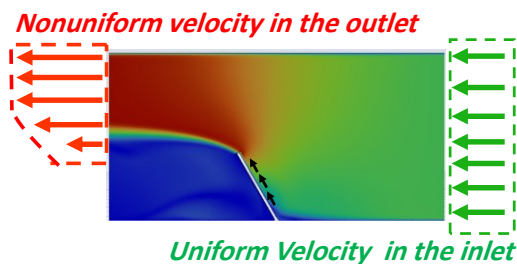


Fig. 14. The velocity contour around the 60° tilted solar panel.

To evaluate the surface coverage by the dust particles, it is assumed that the wind speed is 5 m/s and the medium contains dust particles with a volume fraction of $(1000/\text{cm}^3)$. Also, the Stokes law is considered to evaluate the falling speed of the dust particles as provided by Eq.5 [36,37].

$$v_s = \frac{(\rho_s - \rho_f)gd^2}{18\mu} \quad (5)$$

In Eq.5, ρ_s and ρ_f represents the density of dust particles (2.2 g/cm^3) and the density of air, respectively. g is the gravitational acceleration, and μ is the dynamic viscosity of air.

Based on these factors, for a wind speed of 5 m/s, the area covered by the solar panel after 5 minutes is estimated to be 131.41% which indicates 31.41% of the surface is covered by dust particles, twice the rest of it. This coverage ratio assumes that no dust particles are repelled from the surface, serving as a benchmark to compare scenarios with and without the anti-soiling coating. On the other hand, Table.3 shows the coverage evolves within this duration obtained numerically. Additionally, the results achieved are experimentally confirmed, as shown in the third column of the table. It is important to note that, for this validation, a non-coated glass was used; however, not all dust particles adhere to it. As a result, some deviation from the numerical results should be anticipated. The results of this investigation are presented in Table.3.

Table.3. The comparison of numerical and experimental investigations of dust settlement on the solar panel illustrated in Fig.14.

Time (min)	Coverage (%) (Numerical value)	Coverage (%) (Experimental value)
0.5	13.15	10.16
1	26.27	22.36
1.5	39.45	34.59
2	52.56	48.82
2.5	65.50	61.29
3	78.75	77.23
3.5	92.13	91.48
4	100.00	93.47
4.5	100.00	95.36
5	100.00	97.59

Therefore, using wind blowing can result in dust repulsion from the surface. The setup illustrated in Fig.15 is used to determine the potential of the drag force to remove dust particles from the surface after 4 minutes.

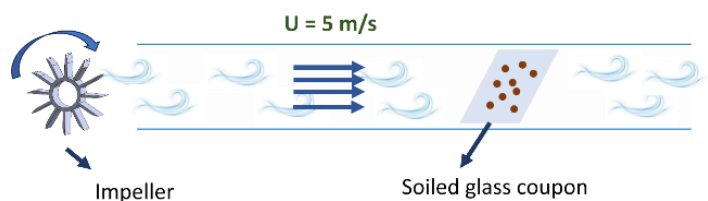


Fig.15. The setup used to detach dust particles from the soiled glass substrate.

After the illustrated operation in Fig.15, the glass substrates were used for image processing endeavors.

The image processing technique revealed a significant ratio of dust repulsion which as reported Table.4. This table describes 6 cycles of the wind blowing procedure, each of which is performed with the previous glass substrate, which has gone through another soiling interval without any further cleansing.

Table.4. The soiling ratio of the coated substrate after each blowing interval.

Number of cycles	(100 - Soiling ratio) %
1	93.47%
2	92.21%
3	91.31%
4	89.86%
5	88.97%
6	87.99%

6. Conclusion

This study presented the design, synthesis, and performance evaluation of a hybrid single-layer anti-soiling coating for solar photovoltaic (PV) modules. The coating, synthesized via a sol-gel process using TEOS, zinc acetate, MEA, and aluminum nitrate, was deposited evenly by a controlled dip-coating method. Morphological and optical characterization confirmed that the resulting layer was thin, homogeneous, and optically transparent, with 85.20% average transmittance across the 350–1000 nm spectrum, crucial to maintaining solar panel efficiency. To evaluate anti-soiling ability, two concurrent mechanisms were investigated: electrostatic repulsion and wind-induced particle ejection. When subjected to a 50 kV/m electric field, the Resistance Coefficient (Ω) increased gradually throughout six test cycles, from 93.0% during the first cycle to 97.1% during the sixth, exhibiting predictable and reproducible repulsion of dust without the need for mechanical cleaning. For passive removal, aerodynamic simulations demonstrated that drag forces on the dust particles increased heavily with particle size and wind speed. At a 5 m/s wind speed, the larger particles (10 μ m radius) experienced greater drag forces, confirming increased detachment at natural wind conditions. Image analysis of six wind-facilitated cleaning cycles also illustrated the durability of the coating: surface cleanliness was only slightly decreased, from 93.47% to 87.99%, during six cycles, indicating resistance to repeated soiling. In addition, deposition simulation under a 60°-tilted panel condition with 5 m/s dusty flow pre-predicted dense dust deposition (131.41%) in the absence of particle repulsion. Experimental results on uncoated glass (116.63%) validated the necessity of active coatings in actual environments. To ensure the reliability of the experimental and numerical findings, an uncertainty analysis was carried out for all key measurements and derived parameters. For optical transmittance measurements (UV–Vis

spectrophotometry, 200–1000 nm range), the instrument manufacturer specifies a baseline noise level of $\pm 0.3\%$ and wavelength accuracy of ± 0.5 nm. Multiple measurements ($n = 5$) were taken for each sample and averaged, with the standard deviation reported as the measurement uncertainty. In the FE–SEM thickness estimation, the main source of error arose from resolution limits and image thresholding; repeated cross-sectional imaging gave a variation of ± 3.5 nm for the silica-based coating layer.

In the mechanical abrasion tests, uncertainties were introduced by small variations in applied normal load and reciprocation length. These were minimized by using calibrated weights (tolerance ± 0.05 g) and a fixed 10 cm stroke length, but a combined relative uncertainty of $\pm 2\%$ was still considered when calculating the abrasion cycle effects. For electrical dust repulsion, variation in applied electric field strength was ± 0.5 kV/m due to power supply regulation, and environmental factors such as ambient humidity ($\sim 3\%$ fluctuation) were monitored, as they influence electrostatic forces.

In the wind-induced dust mitigation tests, the wind speed controller had a tolerance of ± 0.05 m/s, and image-processing-based soiling ratio determination carried a segmentation-related uncertainty of $\pm 1.2\%$, estimated by comparing automated detection with manual pixel counting for selected frames. For the numerical simulations, uncertainties stemmed from assumed particle sphericity, uniform density (2.2 g/cm³), and the neglect of near-wall viscous effects. Sensitivity tests varying particle density by $\pm 5\%$ and drag coefficient correlations by $\pm 3\%$ were performed, showing less than 4% change in predicted surface coverage. Overall, the combined uncertainty for the main reported quantities (optical transmittance, abrasion resistance, dust removal efficiency, and predicted surface coverage) was within $\pm 5\%$. This level of uncertainty does not alter the main conclusions of the study, as the observed performance enhancements between the coated and uncoated samples were significantly larger than the measurement uncertainties.

In summary, the hybrid coating combines passive surface engineering and active electrostatic repulsion in a low-cost, scalable solution to dust suppression for PV systems. Due to its high optical transparency, two-mode cleaning functionality, and environmental stress tolerance, the technology is particularly well-suited to the dry and semi-arid climates. The cross-disciplinary approach (interfacing material science, fluid mechanics, and electrical engineering) holds much potential for maximizing the efficiency and life performance of solar energy technologies.

Nomenclature

FE-SEM	Field Emission Scanning Electron Microscopy
HCl	Hydrochloric Acid
MEA	Monoethanolamine
PV	Photovoltaic

TEOS	Tetraethyl Orthosilicate
UV-Vis	Ultraviolet-Visible Spectrophotometer

μ	Dynamic viscosity of air	Pa·s
ρ	Density	kg·m ⁻³
σ	Surface tension	N·m ⁻¹
Ω	Resistance coefficient (optical clarity ratio)	%

Latin Symbols

Symbol	Definition	Unit
A	Cross-sectional area of particle	m ²
C _D	Drag coefficient	—
C _p	Pressure coefficient	—
d	Particle diameter	m
dA	Differential surface area element	m ²
F _D	Total aerodynamic drag force	N
F _L	Lift force (if applicable in flow field)	N
g	Gravitational acceleration	m·s ⁻²
h	Coating thickness	m
k	Thermal or material conductivity (when applicable)	W·m ⁻¹ ·K ⁻¹
m	Particle mass	kg
n	Number of each interval in Fig. 11	—
r	Particle radius	m
t	Time	s
u	Flow velocity component	m·s ⁻¹
U	Free-stream wind velocity	m·s ⁻¹
V	Volume of a dust particle	m ³
V _s	Settling velocity from Stokes' law	m·s ⁻¹

Greek Symbols

Symbol	Definition	Unit
β	Angular position on the particle surface	rad or °
Δ	Difference/variation in a parameter	— or depends
ε	Measurement error/uncertainty	% or as given
η	Efficiency (optical, dust removal, etc.)	%
λ	Wavelength of light	nm

Dimensionless Numbers

Symbol	Definition	Unit
Re	Reynolds number	—
St	Stokes number	—

Ethics Approval

The scientific content of this article is the result of the authors' research and has not been published in any Iranian or international journal.

Conflict of Interest

The authors declare that they have no conflicts of interest to this work.

References

- [1] M.B. Hayat, D. Ali, K.C. Monyake, L. Alagha, N. Ahmed, Solar energy—A look into power generation, challenges, and a solar-powered future, *Int J Energy Res* 43 (2019) 1049–1067. <https://doi.org/10.1002/er.4252>.
- [2] M. Minaei, S. Faghiri, J. Ranjbar Kermani, A. Riahi, M. Behshad Shafii, A novel solar-driven vacuum desalination unit: Simultaneously venturi-induced self-evaporation and self-condensation with fresh water cycle, *Solar Energy* 282 (2024) 112889. <https://doi.org/10.1016/J.SOLENER.2024.112889>.
- [3] P. Hooshyar, A. Moosavi, A.N. Borujerdi, Enhanced dust reduction method for solar panels application, *Sci Rep* 14 (2024). <https://doi.org/10.1038/s41598-024-81183-7>.
- [4] C. Liu, H. Li, F. Zhang, X. Wang, Improvement on the passive method based on dampers for the vibration control of spacecraft solar panels, *Advances in Mechanical Engineering* 14 (2022) 1–16. <https://doi.org/10.1177/16878132221080596>.
- [5] B. Wu, X. Cui, H. Jiang, N. Wu, C. Peng, Z. Hu, X. Liang, Y. Yan, J. Huang, D. Li, A superhydrophobic coating harvesting mechanical robustness, passive anti-icing and active de-icing performances, *J Colloid Interface Sci* 590 (2021) 301–310. <https://doi.org/10.1016/J.JCIS.2021.01.054>.
- [6] L.B. Bosman, W.D. Leon-Salas, W. Hutzl, E.A. Soto, PV system predictive maintenance: Challenges, current approaches, and opportunities, *Energies (Basel)* 16 (2020). <https://doi.org/10.3390/en13061398>.
- [7] G.E. Cohen, D.W. Kearney, G.J. Kolb, Final report on the operation and maintenance segs.pdf, (1999).
- [8] M. Može, V. Vajc, M. Zupančič, I. Golobič, Hydrophilic and hydrophobic nanostructured

- copper surfaces for efficient pool boiling heat transfer with water, water/butanol mixtures and novac 649, *Nanomaterials* 11 (2021). <https://doi.org/10.3390/nano11123216>.
- [9] P. Bellmann, F. Wolfertstetter, R. Conceição, H.G. Silva, Comparative modeling of optical soiling losses for CSP and PV energy systems, *Solar Energy* 197 (2020) 229–237. <https://doi.org/10.1016/j.solener.2019.12.045>.
- [10] C.I. Calle, C.R. Buhler, M.R. Johansen, M.D. Hogue, S.J. Snyder, Active dust control and mitigation technology for lunar and Martian exploration, *Acta Astronaut* 69 (2011) 1082–1088. <https://doi.org/10.1016/j.actaastro.2011.06.010>.
- [11] S. Bhaduri, M. Farkade, R. Bajhal, S. Mallick, N. Shiradkar, A. Kottantharayil, Impact of different brush designs in robotic cleaning on the degradation of anti-soiling coatings, *Conference Record of the IEEE Photovoltaic Specialists Conference* (2021) 2434–2438. <https://doi.org/10.1109/PVSC43889.2021.9519046>.
- [12] D. Helmer, N. Keller, F. Kotz, F. Stolz, C. Greiner, T.M. Nargang, K. Sachsenheimer, B.E. Rapp, Transparent, abrasion-insensitive superhydrophobic coatings for real-world applications, *Sci Rep* 7 (2017). <https://doi.org/10.1038/s41598-017-15287-8>.
- [13] C. Neinhuis, W. Barthlott, Characterization and distribution of water-repellent, self-cleaning plant surfaces, *Ann Bot* 79 (1997) 667–677. <https://doi.org/10.1006/anbo.1997.0400>.
- [14] G.P. Smestad, T.A. Germer, H. Alrashidi, E.F. Fernández, S. Dey, H. Brahma, N. Sarmah, A. Ghosh, N. Sellami, I.A.I. Hassan, M. Desouky, A. Kasry, B. Pesala, S. Sundaram, F. Almonacid, K.S. Reddy, T.K. Mallick, L. Micheli, Modelling photovoltaic soiling losses through optical characterization, *Sci Rep* 10 (2020). <https://doi.org/10.1038/s41598-019-56868-z>.
- [15] A. Sayyah, M.N. Horenstein, M.K. Mazumder, Mitigation of soiling losses in concentrating solar collectors, in: 2013 IEEE 39th Photovoltaic Specialists Conference (PVSC), IEEE, 2013: pp. 480–485.
- [16] L. Wang, J. Liu, C. Yang, D. Wu, A novel interval dynamic reliability computation approach for the risk evaluation of vibration active control systems based on PID controllers, *Appl Math Model* 92 (2021) 422–446. <https://doi.org/10.1016/j.apm.2020.11.007>.
- [17] C. Kammeyer, R. Hamilton, J. Morrison, Averting the global water crisis: three considerations for a new decade of water governance, *Georgetown Journal of International Affairs* 21 (2020) 105–113.
- [18] A.A. Abubakar, B.S. Yilbas, H. Al-Qahtani, A. Alzaydi, S. Alhelou, Environmental dust repelling from hydrophobic and hydrophilic surfaces under vibrational excitation, *Sci Rep* 10 (2020). <https://doi.org/10.1038/s41598-020-71356-5>.
- [19] R. Nitano, S. Mitsunaga, S. Yamato, K. Tanaka, H. Kanamori, M. Adachi, Cleaning performance of an electrodynamic dust shield under low-frequency vibrations, *Powder Technol* 457 (2025) 120845. <https://doi.org/10.1016/J.POWTEC.2025.120845>.
- [20] M.Z. Al-Badra, M.S. Abd-Elhady, H.A. Kandil, A novel technique for cleaning PV panels using antistatic coating with a mechanical vibrator, *Energy Reports* 6 (2020) 1633–1637.
- [21] M. Memiche, C. Bouzian, A. Benzahia, A. Moussi, Effects of dust, soiling, aging, and weather conditions on photovoltaic system performances in a Saharan environment—Case study in Algeria, *Global Energy Interconnection* 3 (2020) 60–67. <https://doi.org/10.1016/J.GLOEI.2020.03.004>.
- [22] M.R. Maghami, H. Hizam, C. Gomes, M.A. Radzi, M.I. Rezadad, S. Hajighorbani, Power loss due to soiling on solar panel: A review, *Renewable and Sustainable Energy Reviews* 59 (2016) 1307–1316. <https://doi.org/10.1016/j.rser.2016.01.044>.
- [23] S. Bhaduri, R. Bajhal, S. Mallick, N. Shiradkar, A. Kottantharayil, Degradation of anti-soiling coatings: Mechanical impact of rainfall, *Conference Record of the IEEE Photovoltaic Specialists Conference 2020-June* (2020) 1098–1101. <https://doi.org/10.1109/PVSC45281.2020.9300414>.
- [24] J. Wette, F. Sutter, A. Fernández-García, Evaluation of anti-soiling coatings for CSP reflectors under realistic outdoor conditions, *Solar Energy* 191 (2019) 574–584. <https://doi.org/10.1016/j.solener.2019.09.031>.
- [25] J. Wette, A. Fernández-García, F. Sutter, F. Buendía-Martínez, D. Argüelles-Arízun, I. Azpitarte, G. Pérez, Water saving in CSP plants by a novel hydrophilic anti-soiling coating for solar reflectors, *Coatings* 9 (2019). <https://doi.org/10.3390/coatings9110739>.
- [26] J. Khan, M.H. Arsalan, Solar power technologies for sustainable electricity generation—A review, *Renewable and Sustainable Energy Reviews* 55 (2016) 414–425.
- [27] S. Mekhilef, R. Saidur, A. Safari, A review on solar energy use in industries, *Renewable and Sustainable Energy Reviews* 15 (2011) 1777–1790. <https://doi.org/10.1016/j.rser.2010.12.018>.
- [28] D.S. Bhatkhande, V.G. Pangarkar, A.A.C.M. Beenackers, Photocatalytic degradation for environmental applications—a review, *Journal of Chemical Technology & Biotechnology: International Research in Process, Environmental & Clean Technology* 77 (2002) 102–116.
- [29] A. Shaju, R. Chacko, Soiling of photovoltaic modules- Review, in: *IOP Conf Ser Mater Sci Eng*, Institute of Physics Publishing, 2018. <https://doi.org/10.1088/1757-899X/396/1/012050>.
- [30] M. Li, Y. Li, F. Xue, X. Jing, A robust and versatile superhydrophobic coating: Wear-resistance study upon sandpaper abrasion, *Appl Surf Sci* 480 (2019) 738–748. <https://doi.org/10.1016/j.apsusc.2019.03.001>.

- [31] M. Li, Y. Li, F. Xue, X. Jing, A robust and versatile superhydrophobic coating: Wear-resistance study upon sandpaper abrasion, *Appl Surf Sci* 480 (2019) 738–748. <https://doi.org/10.1016/j.apsusc.2019.03.001>.
- [32] F. Su, K. Yao, Facile fabrication of superhydrophobic surface with excellent mechanical abrasion and corrosion resistance on copper substrate by a novel method, *ACS Appl Mater Interfaces* 6 (2014) 8762–8770. <https://doi.org/10.1021/am501539b>.
- [33] F. Su, K. Yao, Facile fabrication of superhydrophobic surface with excellent mechanical abrasion and corrosion resistance on copper substrate by a novel method, *ACS Appl Mater Interfaces* 6 (2014) 8762–8770. <https://doi.org/10.1021/am501539b>.
- [34] S. Panat, K.K. Varanasi, Electrostatic dust removal using adsorbed moisture–assisted charge induction for sustainable operation of solar panels, *Sci Adv* 8 (2022) eabm0078.
- [35] J. Wang, D.D. Joseph, Potential flow of a second-order fluid over a sphere or an ellipse, *J Fluid Mech* 511 (2004) 201–215. <https://doi.org/10.1017/S0022112004009541>.
- [36] K. Vajravelu, S. Mukhopadhyay, Flow past a sphere, *Fluid Flow, Heat and Mass Transfer At Bodies of Different Shapes* (2016) 145–152. <https://doi.org/10.1016/B978-0-12-803733-1.00006-5>.
- [37] NII-Electronic Library Service, Teruo KUMAGAI, Akihide KOBAYASHI. <https://doi.org/10.1299/jsme1958.28.1925>.